Molecular-Level Analysis of the Wetting Behavior of Imidazolium-Based Ionic Liquids on Bismuth Telluride Surfaces

Henry Atkinson, Jason E. Bara, and C. Heath Turner*

Department of Chemical and Biological Engineering, The University of Alabama, Box 870203,

Tuscaloosa, Alabama 35487, USA

Abstract

Bismuth telluride is among the most studied thermoelectric materials. Its performance, which is among the highest around room temperature, is dependent on exfoliation to thin nanosheets. While previous research has examined the exfoliation mechanism by ionic liquids (ILs), this study provides more detailed information about the solid-liquid interface, including predicted values for IL contact angles (θ) on Bi_2Te_3. Molecular dynamics simulations are employed to compute θ and other properties of interest, including mass and charge ordering, adsorption energy, and electrostatic potential. All properties save the latter are strongly dependent on anion size and slightly dependent on cation size. The IL contact angles display a wide range of values, from 97.7° for the smallest ions to 53.2° for the largest ions. An analysis of the molecular-level interactions in these systems serves to explain this behavior, and they indicate that reduced cohesive interactions in bulkier liquids are primarily responsible.

Keywords: interface; surface tension; contact angle; thermoelectric; molecular dynamics; solvation

*Corresponding author: hturner@eng.ua.edu
(205) 348-1733 (phone)
(205) 348-7558 (fax)

1. Introduction

Bismuth telluride (Bi_2Te_3) and its alloys are among the longest studied thermoelectric materials, with applications in power generation (the Seebeck effect) and solid-state cooling (the Peltier effect).[1-4] The efficiency of thermoelectric materials is quantified by their dimensionless figure of merit (ZT), which must be greater than 3 or 4 for widespread practical use.[5] Bi_2Te_3 has the highest ZT near room temperature among widely-studied thermoelectric materials, but it still remains around 1 in bulk Bi_2Te_3. Recent research has worked to raise this number by decreasing one or more of the material's dimensions to the nanoscale.[6-7] Bi_2Te_3 occurs as 1 nm thick nanosheets composed of covalently bonded atomic layers of Te-Bi-Te-Bi-Te, and these sheets are primarily held together in the bulk material by van der Waals forces. A scalable process is needed that can efficiently exfoliate Bi_2Te_3 into two-dimensional nanosheets without imparting structural defects or impurities. Moreover, due to the growing interest in many other two-dimensional materials (graphene, MoS_2, $MoSe_2$, WSe_2, hBN, TiB, etc.), there is a compelling motivation to develop a better understanding of the interfacial and solvation properties of these materials for future applications.

Various techniques have been employed to separate these nanosheets from the bulk material, including sonication, gas evolution following intercalation, and mechanical separation.[5, 8-11] One experiment used ionic liquids (ILs) for this purpose, and the process was also modeled computationally.[10-11] Ionic liquids are salts characterized by full separation of charges between molecules while remaining liquid at low temperatures. Some of their unique properties include low vapor pressure, high thermal stability, and tunability based on the choice of cations and anions. Additionally, the full charge separation permits different interactions with partially charged species (like Bi_2Te_3) than are possible with traditional solvents.[12-14] Abedini, et al.

investigated the role of ionic liquid choice on Bi_2Te_3 exfoliation via molecular dynamics (MD) simulations and quantified each species' effectiveness in aiding exfoliation.[10] However, those computational details are difficult to directly measure in experiments, and the Bi_2Te_3-IL systems have not been widely characterized.

The details of a solid-liquid interface are often investigated via the contact angle θ, which quantifies the relative interaction strengths between the three phases. The literature is replete with studies of water on surfaces such as metals, silica, carbon allotropes, and polymers,[15-18] including computational comparisons.[17-19] IL wetting behavior has also been extensively studied experimentally,[20-23] but computational results are scarce for these materials, with the earliest molecular-level simulations appearing approximately a decade ago.[24] In MD simulations, substrates for ionic liquid drops have consisted of a relatively small range of materials, including graphene,[25] graphite,[26] Si,[27] poly(ethylene oxide),[28] TiO_2,[29] and BN.[30]

This study examines the contact angles formed by imidazolium-based ILs on a Bi_2Te_3 surface, as well as mass and charge ordering, adsorption energy, and electrostatic potential. In general, these properties display a wide range of values, which are strongly dependent on anion size but slightly dependent on cation size. An analysis of the molecular-level interactions in these systems serves to explain this behavior and provides critical information about the fundamental interactions in the system that can be used for designing effective exfoliation processes.

2. Simulation Details

Eleven different liquids are studied, including combinations of cations 1-ethyl-3-methylimidazolium ([$emim^+$]) and 1-butyl-3-methylimidazolium ([$bmim^+$]) with anions [Cl^-],

[Br^-], [BF_4^-], [PF_6^-], and bistriflimide ([Tf_2N^-]), as well as water. Each IL drop contains 300 cation-anion pairs, and the water drop contains 2500 molecules to achieve a similar size (approximately 2.6 nm radius). While the finite droplet sizes may slightly affect the predicted contact angles at the nanoscale, it was not computationally practical to simulate a range of droplet sizes for each liquid at a range of temperatures. Additionally, beyond a threshold size for a given system, the contact angle is often much less sensitive to change with size; both the ionic liquid[27, 31] and water droplets[32-33] are at or above the threshold in similar simulations.

In order to build the simulation models, PACKMOL[34] is first used to create cubic boxes with each bulk liquid for initial equilibration, prior to placing the liquids on the Bi_2Te_3 surface. Our MD simulations are performed using GROMACS[35] 4.6.5 with a timestep of 1 fs, and periodic boundary conditions are applied in all three directions. The Lennard-Jones potential is used to model nonbonded interactions with a cutoff of 1.4 nm. The IL force field parameters are taken from OPLS-AA,[36] with modifications by Lopes et al.,[37] and the TIP3P and SPC/E models are used for water for comaprison.[38] We expect that the SPC/E model is more accurate for our interfacial simulations given its more accurate surface tension, though each model has other strengths and weaknesses.[39] Unlike neighbor interactions are calculated via the Lorentz-Berthelot mixing rules. Electrostatic interactions are modeled using the particle-mesh Ewald summation with a cutoff of 1.4 nm, and a reciprocal space parameter of 0.16 nm. Temperature is maintained using the Nosé-Hoover thermostat with a 0.4 ps time constant.

In order to improve equilibration, the IL drops were equilibrated through simulated annealing at constant volume in different stages: (a) the temperature is first increased from 550 K to 1000 K over a period of 100 ps; (b) the temperature is then maintained at 1000 K for 800 ps; and (c) then the temperature is reduced to 550 K over 100 ps. Water is equilibrated via a 1 ns isothermal-

isobaric ensemble (NPT) simulation at 298 K and 1 bar maintained by the Parrinello-Rahman barostat with a time constant of 20 ps. After equilibration, the cubic liquid systems are placed 0.65 nm above the Bi_2Te_3 surface for a canonical (NVT) simulation with the same parameters as above, except that the reciprocal space parameter is increased to 0.32 nm to speed up the simulations in the larger box.

The Bi_2Te_3 surface is constructed by repeating the bulk crystallographic unit cell[40] in the x and y dimensions, with an overall thickness of two quintuple layers (1.768 nm). Additional layers are not added due to increased computational cost and the short-range interaction cutoff of 1.4 nm. It has also been shown that previous studies of phosphorene[32] and MoS_2[41] have approximated the bulk material (for wetting purposes) with thinner substrates than used here. The dimensions of the surface are extended to prevent the liquid drops from interacting with their periodic images; this gave dimensions ranging from 10.11×10.28 nm to 16.26×16.37 nm, and the z dimension was 15 nm. The Bi_2Te_3 sheet is frozen in place, a common simplification[25, 27, 31, 42-43] that reduces computational cost with negligible impact on predicted contact angles for water.[44] The van der Waals interactions between the surface and the liquids are described by the universal force field,[45] and the partial charges are taken from Kullmann, et al.[46]

Once the liquid droplets are placed in contact with the Bi_2Te_3 surface, the systems are equilibrated for an additional 10 ns at 1 bar and 550 K (298 K for the water droplet). The ILs are then simulated at 500 K, 450 K, and 400 K for 5 ns each, with the final 3 ns of each run used for analysis. Since the predicted contact angles did not display any significant temperature sensitivity (Figure S1), additional extended runs of 10 ns are performed only at 450 K. A representative snapshot is shown in Figure 1, along with an illustration of the contact angle applied in our simulation analysis.

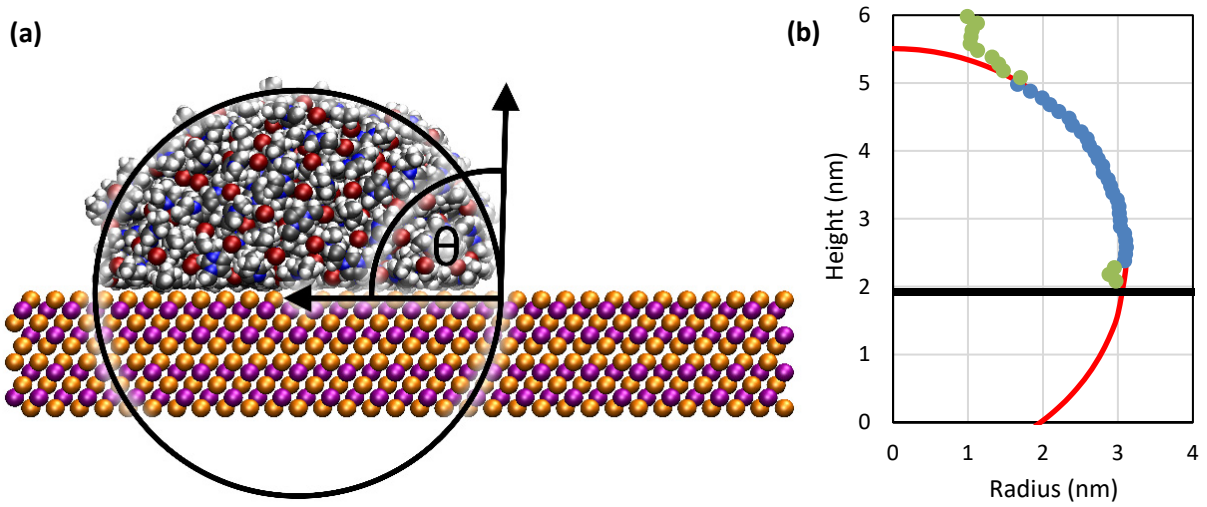

Figure 1. (a) Simulation snapshot of the IL droplet on the two-layer Bi_2Te_3 surface, along with an illustration of the contact angle. The atoms are colored according to their species: Te (orange), Bi (purple), H (white), C (gray), N (blue), Br (red); (b) Illustration of the curve fitting approach applied to the liquid droplet profile, with the uppermost and bottom points (green) discarded from the analysis. The solid black line represents the Bi_2Te_3 surface (defined by the center of the uppermost atoms).

Several different techniques are used to quantify the interactions between the liquid droplets and the Bi_2Te_3 surface. For instance, a circle-fitting technique[47-48] (Figure 1) is used to compute the liquid contact angles with the surface. For each frame in the MD trajectory, the atoms in the droplet are translated in the x-y plane and superimposed so that each frame has the same x-y center of mass (and averages values can be consistently calculated). The droplet is assumed to be spherical, which allows measurement of the radial density profile in discs normal to the Bi_2Te_3 surface. For each layer, the bulk density is computed in the innermost 1 nm radius of the drop, and the edge is defined as the region with density half that of the bulk. Droplet edge points for low density layers are discarded due to poor statistics. Specifically, points with heights below the first density peak at the solid-liquid interface (the lowest points) and the points above the minimum radius (typically 1.0-1.5 nm) are discarded. A least-squares fit is used to generate a fitted circle, and the contact angle is computed as the intersection of the circle with the Bi_2Te_3 surface, defined as the plane of the uppermost atomic centers. Standard deviations for the contact

angle values are computed by dividing the trajectory into four 2.5 ns segments, calculating the contact angle for each, and averaging.

Next, the adsorption energy for the droplets is calculated by comparing the potential energy for the system (U_{sys}) to the potential energies of the drop alone (U_{drop}) and sheet alone (U_{sheet}); the difference between the system's and individual components' energies is defined as the adsorption energy: $U_{ads} = U_{sys} - (U_{drop} + U_{sheet})$. This value is normalized by the droplet-sheet contact area (A_c), giving a normalized energy of $\tilde{U}_{ads} = U_{ads} / A_c$. Standard deviations are calculated by analyzing four 2.5 ns segments, as before.

In order to quantify the molecular-level electrostatic interactions in the system, the electrostatic potential (ESP) is computed for the exposed surface of the liquid droplets (i.e., excluding the Bi_2Te_3 surface). To do this, an atomic probe with a diameter of 0.26 nm (kinetic diameter of helium) is used to sample points on the liquid surface, and the ESP is calculated from the partial atomic charges corresponding to the different atomic sites. The ESP at each point on the surface (approximately 10^6 total samples) is then used to obtain the ESP distribution (averaged over 10 different frames from each system trajectory).

3. Results and Discussion

3.1 Contact Angles

The contact angles of each liquid at 450 K are displayed in Figure 2 (numerical values provided in Table S1). As evident in Figure 1, a smaller contact angle occurs for a more wetting liquid. Experimental results for water's contact angle on Bi_2Te_3 include 51.7°-75.2°[49] and 8°-36°,[50] though both experiments correspond to rough Bi_2Te_3 surfaces, in contrast to the perfect surface modeled in the present study. We expect that the SPC/E contact angle for water is more

accurate because of its surface tension accuaracy, another interfacial property. The trend for the ILs corresponds to the exfoliation performance reported by Abedini et al.,[10] with larger anions (such as [Tf_2N^-]) being both more wetting and more effective solvents for exfoliation. The contact angles of the larger cation ([$bmim^+$]) are always lower, though there is less of a trend in the alkyl chain length versus exfoliation efficiency.[10] Interactions between the liquid and the surface (both for exfoliation and droplet behavior) can be explained by the relative strengths of cohesive (liquid-liquid) and adhesive (liquid-surface) interactions. A liquid displaying increased wetting behavior can be explained by a combination of decreased cohesive forces and increased adhesive forces. We propose, based on the other properties measured, that the behavior is primarily due to decreased cohesion.

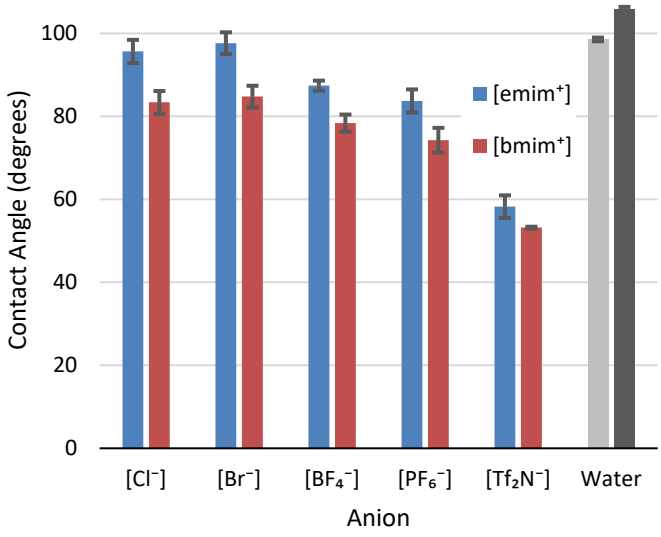

Figure 2. Contact angles at 450 K (298 K for water). Error bars represent standard deviations from averaging four 2.5 ns windows, each with 250 frames. The light gray bar for water shows the TIP3P model's results, and the dark gray bar shows the SPC/E model's results.

3.2 Mass Distribution

Figure 3 displays the normalized mass distribution of the droplets versus distance from the surface. This allows for comparison of the density of the liquids near the surface. The liquids tend not to display significant long-range ion ordering, as evident by the relatively constant densities versus distance in Figure S2; only slight deviations occur. The heights of the first peak in Figure 3(a) show that [Cl^-]- and [Br^-]-containing liquids (with peak heights of 2.0) are more ordered than those with [BF_4^-] or [PF_6^-] (heights of 1.73 and 1.68, respectively), and much more than with [Tf_2N^-] (1.41) close to the surface. The decrease in order is also present with increasing cation size, as shown in Figure 3(b), though the effect is stronger immediately adjacent to the surface and with smaller anions. Specifically, the first peak heights for [$bmim^+$]-containing liquids are as follows: [Cl^-]-1.69, [Br^-]-1.66, [BF_4^-]-1.63, [PF_6^-]-1.59, [Tf_2N^-]-1.38. If larger molecules were more wetting due to increased adhesion, it is expected that they would be denser near the surface due to stronger liquid-surface interactions. However, the opposite trend is observed, which is likely due to reduced cohesion, so the liquid spreads (wetting more) and is less dense (lower peak). Figure 4 directly compares these peak heights to contact angle, showing that the trend is relatively linear. It is not surprising that the trend seems to disappear with very high peaks, since there is an absolute limit on contact angle (180°), while density relative to bulk density is not necessarily limited. Additionally, it is expected that contact angle decreases rapidly just above a peak height of 1, since the linear fit otherwise predicts complete wetting with a peak height of less than 1, which is not reasonable. Finally, the four points ([bmim][Cl], [bmim][Br], and both water models) excluded from the linear regression share the common properties of small molecule size and contact angle greater than 90° (i.e., a non-wetting regime). The latter property is expected to have a stronger impact, since [bmim][Cl] and [bmim][Br] are only slightly larger but fit the regression very well. For the non-wetting fluids, it is assumed that

the fluid structure is more strongly influenced by cohesive interactions than surface interactions, leading to a decay in the linear correlation.

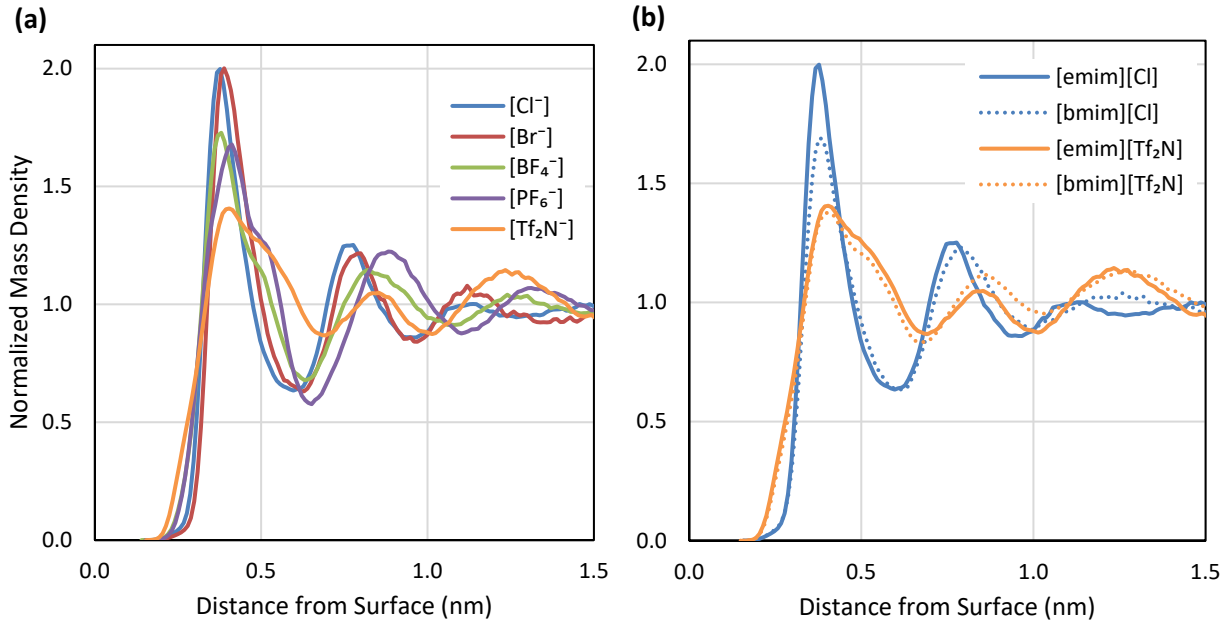

Figure 3. Mass density profiles (total of cation and anion) near the solid-liquid interface. (a) Comparison of anion effects with respect to the [emim$^+$] cation. (b) Comparison of the cation effects for the smallest and largest anions.

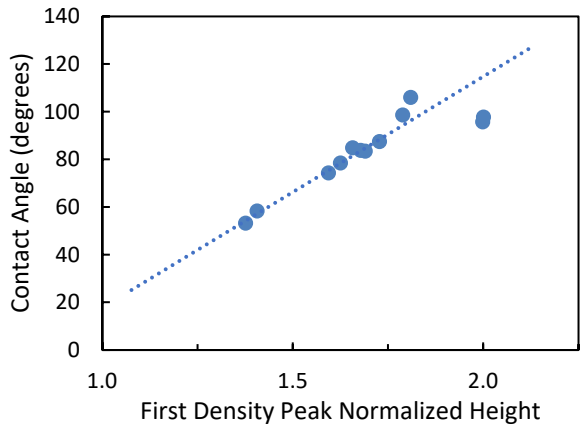

Figure 4. Relationship between contact angle and density distribution perpendicular to the Bi_2Te_3 surface (defined by the height of the first peak of the normalized density). The data correlate linearly ($R^2 = 0.985$) for all but the most strongly ordered liquids ([emim][Cl] and [emim][Br] and water), the four rightmost points, which are excluded from the fit.

3.3 Charge Distribution

The Te (interfacial) atoms on the Bi_2Te_3 surface have a negative partial charge (δ = -0.26 e), which affects the behavior of charged and partially charged atoms in the liquid. It is expected that more adhesive liquids would exhibit high positive charge density near the surface, due to attractive electrostatic interactions. However, Figure 5(a) shows that [Tf_2N^-], the most wetting anion, has high negative charge density close to the surface, so increased Coulombic attraction to the surface is not likely to be responsible for the lower contact angle. Figure 5(b) demonstrates that the attenuating effect of longer cation alkyl chains also occurs for charge density. It should also be noted that larger anions have individual atoms that may reach closer to the surface than the single [Cl^-] or [Br^-] atoms, even when the mass density peak locations are equal. Those negatively charged extremities of the larger anions are responsible for the high negative charge density near the surface in their respective liquids. This is especially evident in Figure 5(c)-(d), which shows that [Cl^-]'s negative charge peak occurs farther from the surface than [Tf_2N^-]'s. Additionally, the charge distribution attenuates quickly with increasing distance, so the droplet-sheet system does not preserve long-range ion order in the liquid.

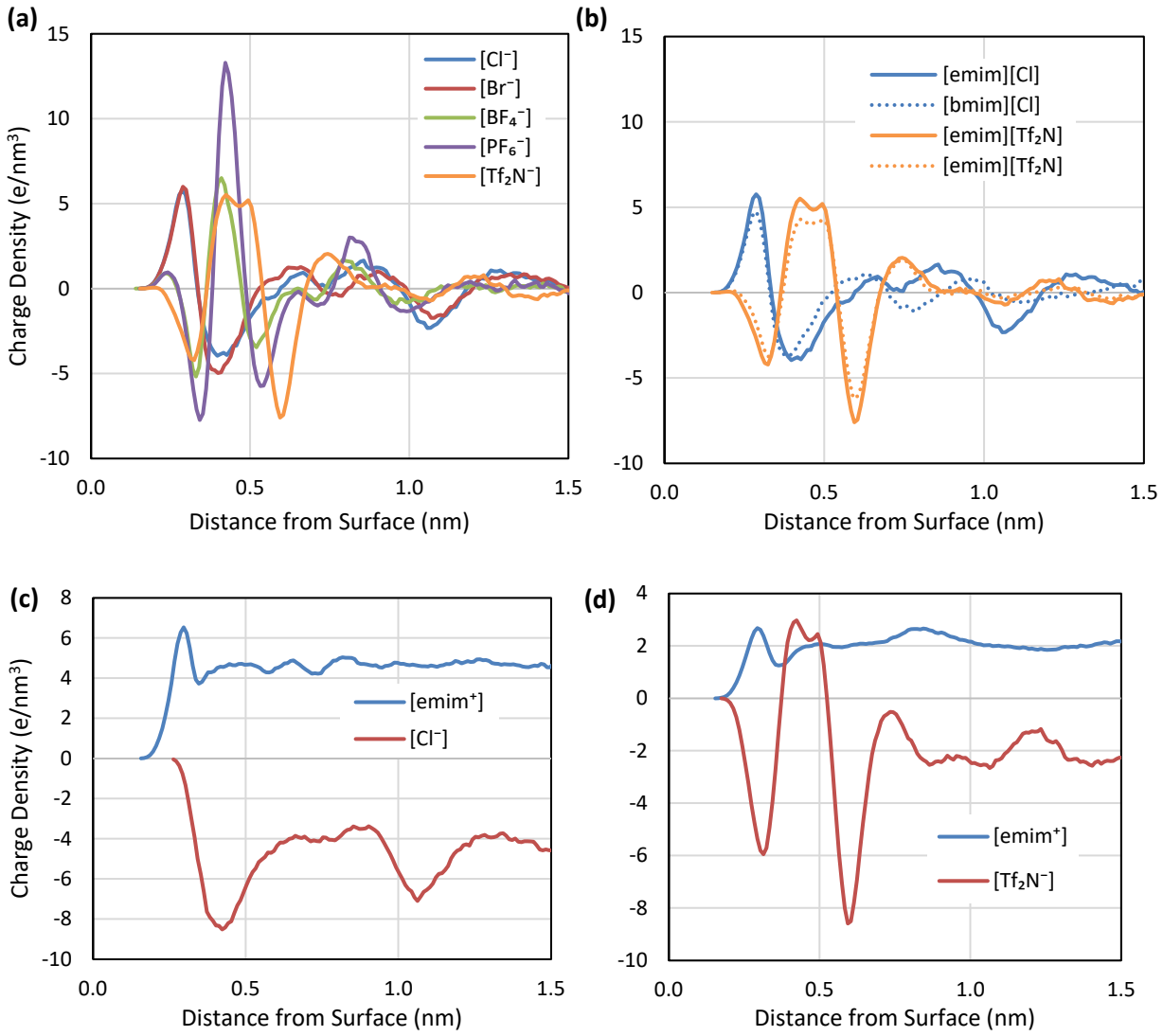

Figure 5. Total charge density profiles in liquids (excluding Bi_2Te_3) near the solid-liquid interface, following the orthogonal distribution method illustrated in Figure 7(a). (a) Comparison of anion effects corresponding to the [emim$^+$] cation. (b) Comparison of cation effects for the smallest and largest anions. (c) Individual ion contributions for [emim][Cl]. (d) Individual ion contributions for [emim][Tf_2N].

The mass and charge distributions in Figures 3 and 5 were calculated in the typical manner by considering the atoms in slices parallel to the surface (Figure 6(a)). On the other hand, the charge distribution near the vacuum-liquid interface was determined using spherical shells centered at the fitted circle's center, as shown in Figure 6(b). Due to the differing sizes of the droplets, the distributions are shifted to begin at the density peak nearest the vacuum interface

instead of at the circle's center. In contrast to the solid-liquid interface, the outer spherical surface of the droplets shows very weak charge ordering for larger anions. The ILs containing [Cl^-] and [Br^-] display multiple distinct peaks in this region (Figure 7a)), mimicking the order at the solid-liquid interface. For the larger anions, the same rough shape is observed (slight positive charge near the edge for [BF_4^-] and [PF_6^-] and slight negative charge for [Tf_2N^-]), though the magnitude is far lower than it is near the surface. The trend of reduction in peak height for the [$bmim^+$] cation is also present in the spherical charge distribution (Figure 7(b)), again showing its tendency to reduce order.

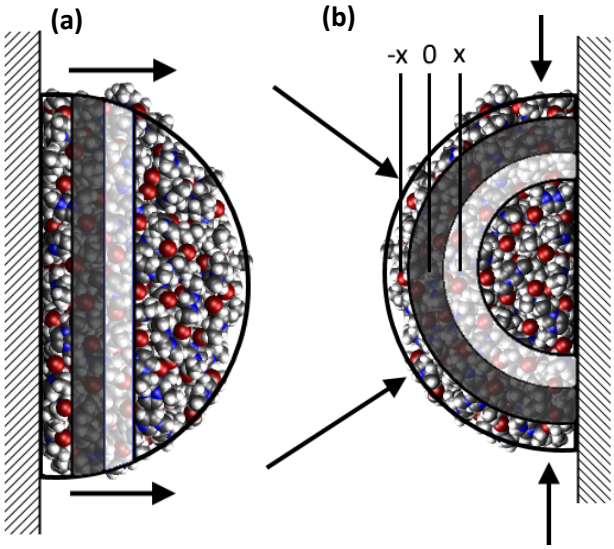

Figure 6. Depictions of charge and mass distribution calculation methods (represented as circles in two dimensions with exaggerated shell thickness for clarity). Arrows show increasing horizontal axis direction in Figures 3, 5, 6. The dark gray regions represent lower distance vales, and the light gray regions represent higher distance values. (a) Orthogonal distribution. (b) Spherical distribution. The 0 distance is value shifted inward for clarity.

(b)

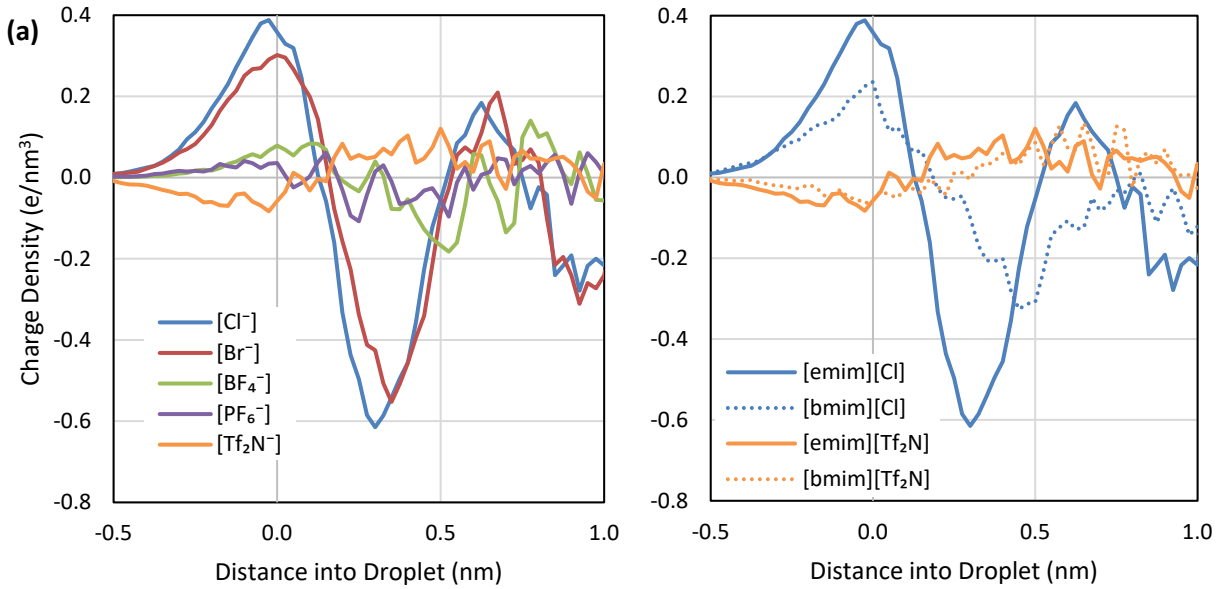

Figure 7. Total charge density profiles in the liquids near the liquid-vacuum interface, following the spherical distribution method illustrated in Figure 6(b). The plots are ordered with the first peak at 0 nm; the zero-density edge occurs around -0.5 nm. (a) Comparison of anion effects on the [emim$^+$] cation. (b) Comparison of cation effects for the smallest and largest anions.

3.4 Adsorption Energy

Figure 8 shows the adsorption energies of the droplets, with a trend similar to that for contact angle. The lower magnitudes of the values for the larger ions mean that they adsorb less strongly to the surface, which is counterintuitive for liquids that have larger contact areas, and it further implies that the reduced cohesion is the primary cause of improved wetting. The experimental surface tension data in Table 1 support this as a more direct measure of cohesive energy, showing that the liquids with larger molecules are less prone to forming a spherical surface (and thus more prone to wetting). Additionally, the decrease in adsorption energy (as opposed to equal energies for each system) could imply that adhesion actually decreases with increased ion size, and that reduced cohesion is even more responsible for the behavior than is initially apparent. The flatter shape of the more wetting droplets may also be responsible, i.e. the contact

area increases, but the thickness of the droplet decreases, possibly to within the interaction range with the sheet. However, such an explanation is likely insufficient for the very large differences in energy between [Tf_2N^-] and [Cl^-], for instance. Again, the SPC/E model for water is likely more accurate, especially given the correlation of surface tension and adsorption energy.

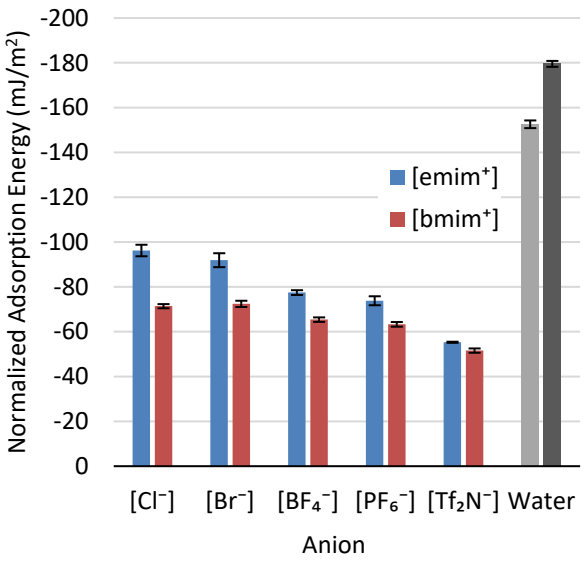

Figure 8. Adsorption energy of liquids calculated from the energies of the droplet alone, surface alone, and droplet-surface system. Standard deviations are from averaging four 2.5 ns windows. The light gray bar for water shows the TIP3P model's results, and the dark gray bar shows the SPC/E model's results.

Table 1. Experimental surface tensions of ILs and water.

Cation	Anion	Surface Tension (mN/m)	450 K Extrapolated Surface Tension (mN/m)
[emim$^+$]	[Cl^-]	62.60 (333 K)[51]	54.16
	[Br^-]	64.40 (348 K)[52]	54.54
	[BF_4^-]	52.05 (298 K), 50.85 (328 K)[53]	45.98
	[PF_6^-]	–	–
	[Tf_2N^-]	35.71 (298 K)[54]	26.58
[bmim$^+$]	[Cl^-]	49.64 (308 K), 47.81 (333 K)[51]	39.96
	[Br^-]	49.98 (308 K), 48.67 (328 K)[52]	40.78
	[BF_4^-]	44.25 (298 K), 42.98 (323 K)[55]	35.60
	[PF_6^-]	44.23 (298 K), 43.19 (323 K)[55]	37.37
	[Tf_2N^-]	33.07 (298 K), 32.11 (323 K)[55]	27.12
Water		71.99 (298 K)[56]	–

The surface tension of a liquid and its contact angle on a surface are often strongly correlated by the Zisman relation.[57] Figure 9 depicts this behavior for the studied liquids using the experimental surface tensions in Table 1; they are extrapolated to 450 K using a linear fit versus temperature, which follows typical IL behavior.[58] The critical surface tension of Bi_2Te_3 (the surface tension of a liquid needed for complete wetting) is estimated as the x-intercept, 6.17 mJ/m^2. Figure S3 shows the Zisman plot of the 450 K contact angles versus surface tensions near 298 K, giving a critical surface tension of 19.27 mJ/m^2 for Bi_2Te_3; if the contact angles change little between 298 K and 450 K, this estimate should be accurate near room temperature. The experimental surface studies by Jian et al.[49] has an estimated surface energy of 22.8-29.5 mJ/m^2 using water as a probe fluid; so the rougher experimental surface does not require as low a liquid surface tension for complete wetting, which is expected.

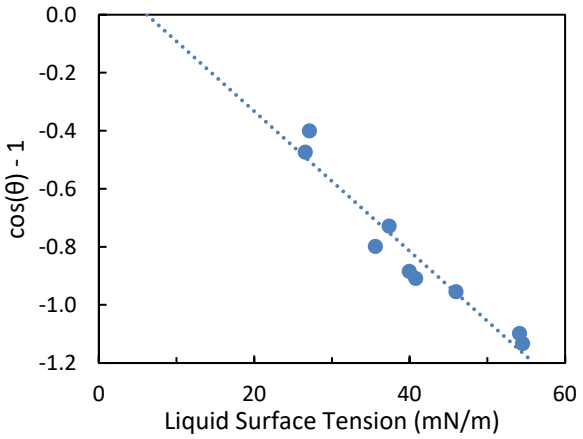

Figure 9. Zisman plot using calculated contact angles and experimental surface tension (extrapolated to 450 K). A linear fit gives a critical surface energy for Bi_2Te_3 of 6.17 mJ/m^2.

3.5 Electrostatic Potential

In contrast to the other properties studied, the electrostatic potential distribution on the droplet surface is nearly equal for all anions (Figure 10(a)). The mean potentials for [emim][Cl] and [emim][Br] are -0.157 V and -0.141 V, respectively, and the larger anions have means of approximately 0 V. The slight negative mean for the halide-containing liquids is surprising given the positive charge ordering both near the solid interface and on the outer spherical edge. On the other hand, the more neutral potential means for the larger anions are to be expected, since they have weaker charge ordering, especially at the spherical edge. Figure 8(b) shows that [bmim$^+$]-containing ILs tend to have a slightly narrower distribution, which is also likely due to reduced charge density. The anions still yield similar distributions with [bmim$^+$], though they tend to be more centered near 0 V. The electrostatic potential distribution on the water surface (centered at -0.093 V) is much wider; however, though water has strong charge ordering near the solid interface, the ordering is relatively weak near the vapor interface. The broader distribution may be due to water's high partial charges compared to the outer atoms in IL molecules. Here,

the water size and potential well parameters are quite similar for both models, so overall droplet structure is likely responsible for the difference.

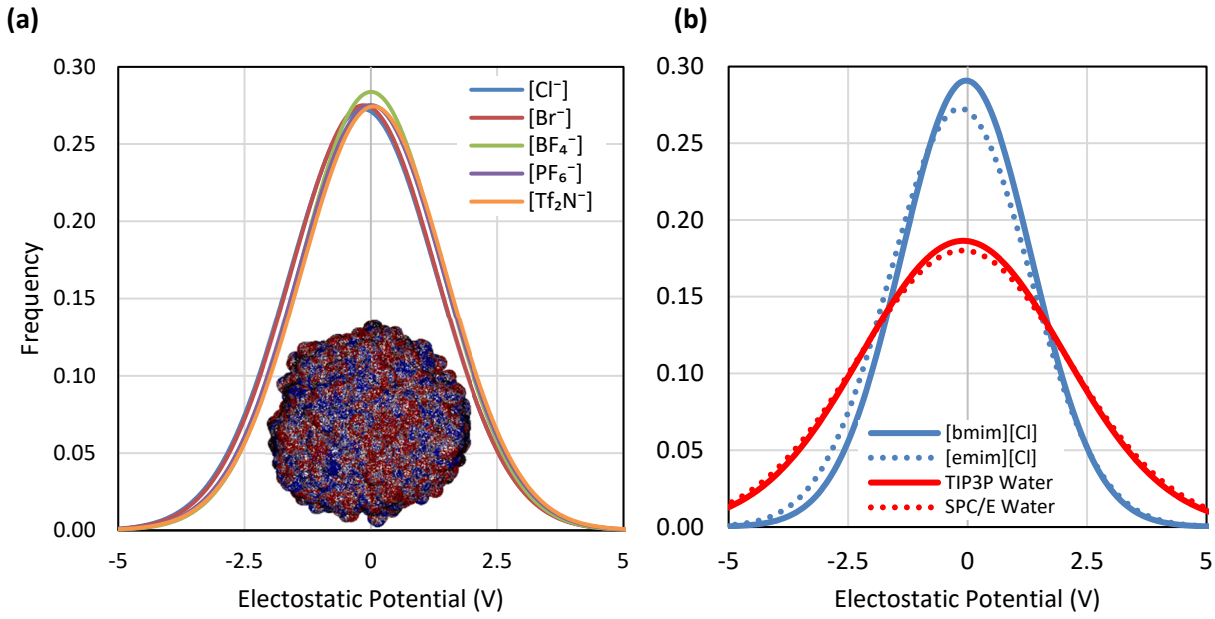

Figure 10. ESP distribution on the droplet surface. Insets depict liquid ESP viewed from above (a) Comparison of anion effects on the [emim$^+$] cation. (b) Comparison of the [emim$^+$] and [bmim$^+$] cations and water models.

4. Conclusion

The interactions of ten different ILs and water with the Bi_2Te_3 surface were studied via MD simulations. The contact angles were observed to decrease with increasing cation and anion size, mirroring the previously reported exfoliation trends.[10] The results of most analyses differed strongly with changing anion size, while the differences between [emim$^+$] and [bmim$^+$] were less pronounced, especially for larger anions. In particular, the charge distribution showed fundamentally different behavior for different anions (both orthogonal to the solid surface and radially, near the liquid-vacuum interface). Atom ordering near the surface also displayed a region of strong correlation with contact angle, with weaker ordering found for more wetting liquids. The adsorption energies of the liquids counterintuitively displayed the same trend as for

the contact angle, which, combined with experimental surface tensions, gave the strongest evidence that reduced cohesion was responsible for the behavior. A Zisman plot was also used to estimate the critical surface energy of Bi_2Te_3 with a good linear fit. Finally, the ESP displayed less sensitivity to the anion, instead showing a narrower distribution (fewer extreme potentials) with increased cation chain length. Water, which was typically between the IL extremes for most other properties, had a very broad ESP distribution, attributed to its relatively high partial charges.

This study has provided the contact angles of various ILs on Bi_2Te_3, which are relatively simple to measure experimentally (compared to the direct exfoliation process). The results act as a computational benchmark for the relatively unstudied interaction of these components, and experimental comparisons have already been made with water, though the roughness of Bi_2Te_3 caused discrepancies even between experiments. Reducing defects in surfaces used for experimental comparison will allow a more accurate comparison to and validation of the computational model, as would further computational studies accounting for surface roughness.

Supporting Information

Supporting information for this article is available. This includes a table with numerical values of the contact angles, the temperature dependence of contact angles, additional density profiles, a Zisman plot, and simulation snapshots.

Acknowledgements

Financial support for this work was provided by the National Science Foundation (CBET-1605411).

References

1. Goldsmid, H. J., Bismuth Telluride and Its Alloys as Materials for Thermoelectric Generation. *Materials* **2014,** *7* (4), 2577-2592.
2. Li, J. F.; Liu, W. S.; Zhao, L. D.; Zhou, M., High-performance nanostructured thermoelectric materials. *Npg Asia Materials* **2010,** *2* (4), 152-158.
3. Li, J. F.; Pan, Y.; Wu, C. F.; Sun, F. H.; Wei, T. R., Processing of advanced thermoelectric materials. *Science China-Technological Sciences* **2017,** *60* (9), 1347-1364.
4. Mamur, H.; Bhuiyan, M. R. A.; Korkmaz, F.; Nil, M., A review on bismuth telluride (Bi2Te3) nanostructure for thermoelectric applications. *Renewable & Sustainable Energy Reviews* **2018,** *82*, 4159-4169.
5. Teweldebrhan, D.; Goyal, V.; Balandin, A. A., Exfoliation and Characterization of Bismuth Telluride Atomic Quintuples and Quasi-Two-Dimensional Crystals. *Nano Letters* **2010,** *10* (4), 1209-1218.
6. Han, C.; Sun, Q.; Li, Z.; Dou, S. X., Thermoelectric Enhancement of Different Kinds of Metal Chalcogenides. *Advanced Energy Materials* **2016,** *6* (15), 1600498.
7. Yang, L.; Chen, Z. G.; Dargusch, M. S.; Zou, J., High Performance Thermoelectric Materials: Progress and Their Applications. *Advanced Energy Materials* **2018,** *8* (6), 1701797.
8. Ding, Z. F.; Bux, S. K.; King, D. J.; Chang, F. L.; Chen, T. H.; Huang, S. C.; Kaner, R. B., Lithium intercalation and exfoliation of layered bismuth selenide and bismuth telluride. *Journal of Materials Chemistry* **2009,** *19* (17), 2588-2592.
9. Ren, L.; Qi, X.; Liu, Y. D.; Hao, G. L.; Huang, Z. Y.; Zou, X. H.; Yang, L. W.; Li, J.; Zhong, J. X., Large-scale production of ultrathin topological insulator bismuth telluride nanosheets by a hydrothermal intercalation and exfoliation route. *Journal of Materials Chemistry* **2012,** *22* (11), 4921-4926.
10. Abedini, A.; Ludwig, T.; Zhang, Z. T.; Turner, C. H., Molecular Dynamics Simulation of Bismuth Telluride Exfoliation Mechanisms in Different Ionic Liquid Solvents. *Langmuir* **2016,** *32* (39), 9982-9992.
11. Ludwig, T.; Guo, L. L.; McCrary, P.; Zhang, Z. T.; Gordon, H.; Quan, H. Y.; Stanton, M.; Frazier, R. M.; Rogers, R. D.; Wang, H. T.; Turner, C. H., Mechanism of Bismuth Telluride Exfoliation in an Ionic Liquid Solvent. *Langmuir* **2015,** *31* (12), 3644-3652.
12. Angell, C. A.; Ansari, Y.; Zhao, Z. F., Ionic Liquids: Past, present and future. *Faraday Discussions* **2012,** *154*, 9-27.
13. Plechkova, N. V.; Seddon, K. R., Applications of ionic liquids in the chemical industry. *Chemical Society Reviews* **2008,** *37* (1), 123-150.
14. Wilkes, J. S., A short history of ionic liquids - from molten salts to neoteric solvents. *Green Chemistry* **2002,** *4* (2), 73-80.
15. Bhushan, B.; Jung, Y. C., Natural and biomimetic artificial surfaces for superhydrophobicity, self-cleaning, low adhesion, and drag reduction. *Progress in Materials Science* **2011,** *56* (1), 1-108.
16. Luzinov, I.; Minko, S.; Tsukruk, V. V., Adaptive and responsive surfaces through controlled reorganization of interfacial polymer layers. *Progress in Polymer Science* **2004,** *29* (7), 635-698.
17. Brutin, D.; Starov, V., Recent advances in droplet wetting and evaporation. *Chemical Society Reviews* **2018,** *47* (2), 558-585.
18. Parobek, D.; Liu, H. T., Wettability of graphene. *2d Materials* **2015,** *2* (3), 032001.
19. Liang, Y. F.; Tsuji, S.; Jia, J. H.; Tsuji, T.; Matsuoka, T., Modeling CO2-Water-Mineral Wettability and Mineralization for Carbon Geosequestration. *Accounts of Chemical Research* **2017,** *50* (7), 1530-1540.
20. Delcheva, I.; Ralston, J.; Beattie, D. A.; Krasowska, M., Static and dynamic wetting behaviour of ionic liquids. *Advances in Colloid and Interface Science* **2015,** *222*, 162-171.
21. Gao, L. C.; McCarthy, T. J., Ionic liquids are useful contact angle probe fluids. *Journal of the American Chemical Society* **2007,** *129* (13), 3804-3805.

22. Kowsari, E.; Payami, M.; Amini, R.; Ramezanzadeh, B.; Javanbakht, M., Task-specific ionic liquid as a new green inhibitor of mild steel corrosion. *Applied Surface Science* **2014,** *289*, 478-486.
23. Paneru, M.; Priest, C.; Sedev, R.; Ralston, J., Static and Dynamic Electrowetting of an Ionic Liquid in a Solid/Liquid/Liquid System. *Journal of the American Chemical Society* **2010,** *132* (24), 8301-8308.
24. Cione, A. M.; Mazyar, O. A.; Booth, B. D.; McCabe, C.; Jennings, G. K., Deposition and Wettability of bmim triflate on Self-Assembled Monolayers. *Journal of Physical Chemistry C* **2009,** *113* (6), 2384-2392.
25. Dong, D. P.; Vatamanu, J. P.; Wei, X. Y.; Bedrov, D., The 1-ethyl-3-methylimidazolium bis(trifluoro-methylsulfonyl)-imide ionic liquid nanodroplets on solid surfaces and in electric field: A molecular dynamics simulation study. *Journal of Chemical Physics* **2018,** *148* (19), 193833.
26. Bordes, E.; Douce, L.; Quitevis, E. L.; Padua, A. A. H.; Gomes, M. C., Ionic liquids at the surface of graphite: Wettability and structure. *Journal of Chemical Physics* **2018,** *148* (19), 193840.
27. Guan, Y. J.; Shao, Q. F.; Chen, W. Q.; Liu, S. M.; Zhang, X. P.; Deng, Y. Q., Dynamic Three-Dimensional Nanowetting Behavior of Imidazolium-Based Ionic Liquids Probed by Molecular Dynamics Simulation. *Journal of Physical Chemistry C* **2017,** *121* (42), 23716-23726.
28. Liu, F. Y.; Lv, Y. X.; Liu, J. J.; Yan, Z. C.; Zhang, B. Q.; Zhang, J.; He, J. S.; Liu, C. Y., Crystallization and Rheology of Poly(ethylene oxide) in Imidazolium Ionic Liquids. *Macromolecules* **2016,** *49* (16), 6106-6115.
29. Malali, S.; Foroutan, M., Study of Wetting Behavior of BMIM+/PF6- Ionic Liquid on TiO2 (110) Surface by Molecular Dynamics Simulation. *Journal of Physical Chemistry C* **2017,** *121* (21), 11226-11233.
30. Ghalami, F.; Sedghamiz, T.; Sedghamiz, E.; Khashei, F.; Zahedi, E., Molecular Dynamics Simulation of Wetting and Interfacial Properties of Multicationic Ionic Liquid Nanodroplets on Boron Nitride Monolayers: A Comparative Approach. *Journal of Physical Chemistry C* **2019,** *123* (22), 13551-13560.
31. Burt, R.; Birkett, G.; Salanne, M.; Zhao, X. S., Molecular Dynamics Simulations of the Influence of Drop Size and Surface Potential on the Contact Angle of Ionic-Liquid Droplets. *Journal of Physical Chemistry C* **2016,** *120* (28), 15244-15250.
32. Chen, S.; Cheng, Y.; Zhang, G.; Pei, Q. X.; Zhang, Y. W., Anisotropic Wetting Characteristics of Water Droplets on Phosphorene: Roles of Layer and Defect Engineering. *Journal of Physical Chemistry C* **2018,** *122* (8), 4622-4627.
33. Zhang, J.; Zhong, J.; Li, W.; Wang, M. H.; Liu, B.; Li, Z.; Yan, Y. G., Molecular insight into the dynamical adsorption behavior of nanoscale water droplets on a heterogeneous surface. *Rsc Advances* **2015,** *5* (65), 52322-52329.
34. Martinez, L.; Andrade, R.; Birgin, E. G.; Martinez, J. M., PACKMOL: A Package for Building Initial Configurations for Molecular Dynamics Simulations. *Journal of Computational Chemistry* **2009,** *30* (13), 2157-2164.
35. Pronk, S.; Pall, S.; Schulz, R.; Larsson, P.; Bjelkmar, P.; Apostolov, R.; Shirts, M. R.; Smith, J. C.; Kasson, P. M.; van der Spoel, D.; Hess, B.; Lindahl, E., GROMACS 4.5: a high-throughput and highly parallel open source molecular simulation toolkit. *Bioinformatics* **2013,** *29* (7), 845-854.
36. Jorgensen, W. L.; Maxwell, D. S.; TiradoRives, J., Development and testing of the OPLS all-atom force field on conformational energetics and properties of organic liquids. *Journal of the American Chemical Society* **1996,** *118* (45), 11225-11236.
37. Lopes, J. N. C.; Deschamps, J.; Padua, A. A. H., Modeling ionic liquids using a systematic all-atom force field. *Journal of Physical Chemistry B* **2004,** *108* (6), 2038-2047.
38. Jorgensen, W. L.; Chandrasekhar, J.; Madura, J. D.; Impey, R. W.; Klein, M. L., Comparison of simple potential functions for simulating liquid water. *Journal of Chemical Physics* **1983,** *79* (2), 926-935.
39. Vega, C.; Abascal, J. L. F., Simulating water with rigid non-polarizable models: a general perspective. *Physical Chemistry Chemical Physics* **2011,** *13* (44), 19663-19688.

40. Feutelais, Y.; Legendre, B.; Rodier, N.; Agafonov, V., A study of the phases in the bismuth - tellurium system. *Materials Research Bulletin* **1993,** *28* (6), 591-596.
41. Leroy, F., Revisiting the droplet simulation approach to derive force-field parameters for water on molybdenum disulfide from wetting angle measurements. *Journal of Chemical Physics* **2016,** *145* (16), 164705.
42. Andrews, J. E.; Sinha, S.; Chung, P. W.; Das, S., Wetting dynamics of a water nanodrop on graphene. *Physical Chemistry Chemical Physics* **2016,** *18* (34), 23482-23493.
43. Hung, S. W.; Shiomi, J., Dynamic Wetting of Nanodroplets on Smooth and Patterned Graphene-Coated Surface. *Journal of Physical Chemistry C* **2018,** *122* (15), 8423-8429.
44. Werder, T.; Walther, J. H.; Jaffe, R. L.; Halicioglu, T.; Koumoutsakos, P., On the water-carbon interaction for use in molecular dynamics simulations of graphite and carbon nanotubes. *Journal of Physical Chemistry B* **2003,** *107* (6), 1345-1352.
45. Rappe, A. K.; Casewit, C. J.; Colwell, K. S.; Goddard, W. A.; Skiff, W. M., UFF, a full periodic-table force-field for molecular mechanics and molecular-dynamics simulations. *Journal of the American Chemical Society* **1992,** *114* (25), 10024-10035.
46. Kullmann, W.; Eichhorn, G.; Rauh, H.; Geick, R.; Eckold, G.; Steigenberger, U., Lattice-dynamics and phonon-dispersion in the narrow gap semiconductor Bi2Te3 with sandwich structure. *Physica Status Solidi B-Basic Research* **1990,** *162* (1), 125-140.
47. De Coninck, J.; Blake, T. D., Wetting and molecular dynamics simulations of simple liquids. *Annual Review of Materials Research* **2008,** *38*, 1-22.
48. Lundgren, M.; Allan, N. L.; Cosgrove, T., Wetting of water and water/ethanol droplets on a non-polar surface: A molecular dynamics study. *Langmuir* **2002,** *18* (26), 10462-10466.
49. Jian, S. R.; Le, P. H.; Luo, C. W.; Juang, J. Y., Nanomechanical and wettability properties of Bi2Te3 thin films: Effects of post-annealing. *Journal of Applied Physics* **2017,** *121* (17), 175302.
50. Thorat, J. B.; Mohite, S. V.; Bagade, A. A.; Shinde, T. J.; Fulari, V. J.; Rajpure, K. Y.; Shinde, N. S., Nanocrystalline Bi2Te3 thin films synthesized by electrodeposition method for photoelectrochemical application. *Materials Science in Semiconductor Processing* **2018,** *79*, 119-126.
51. Souckova, M.; Klomfar, J.; Patek, J., Group contribution and parachor analysis of experimental data on density and surface tension for members of the homologous series of 1-C-n-3-methylimidazolium chlorides. *Fluid Phase Equilibria* **2017,** *454*, 43-56.
52. Klomfar, J.; Souckova, M.; Patek, J., Experimental densities and surface tension and models generating the best-current-knowledge values of them for members of 1-C-n-3-methylimidazolium bromide homologous series. *Journal of Chemical Thermodynamics* **2018,** *118*, 225-234.
53. Shojaeian, A., Surface tension measurements of aqueous 1-alkyle-3-methylimidazolume tetrafluoroborate { C(n)mim BF4 (n=2, 4, 6)} solutions and modeling surface tension of ionic liquid binary mixtures using six various models. *Thermochimica Acta* **2019,** *673*, 119-128.
54. Wandschneider, A.; Lehmann, J. K.; Heintz, A., Surface tension and density of pure ionic liquids and some binary mixtures with 1-propanol and 1-butanol. *Journal of Chemical and Engineering Data* **2008,** *53* (2), 596-599.
55. Li, Z.; Sun, Y.; Zhao, D.; Zhuang, Y.; Wang, R.; Yang, F.; Liu, X. W.; Chen, Y. H., Surface tension of binary mixtures of (ionic liquid plus tributyl phosphate). *Journal of Chemical Thermodynamics* **2019,** *132*, 214-221.
56. Vargaftik, N. B.; Volkov, B. N.; Voljak, L. D., International tables of the surface-tension of water. *Journal of Physical and Chemical Reference Data* **1983,** *12* (3), 817-820.
57. Zisman, W. A., Relation of the Equilibrium Contact Angle to Liquid and Solid Constitution. In *Contact Angle, Wettability, and Adhesion*, American Chemical Society: 1964; Vol. 43, pp 1-51.
58. Tariq, M.; Freire, M. G.; Saramago, B.; Coutinho, J. A. P.; Lopes, J. N. C.; Rebelo, L. P. N., Surface tension of ionic liquids and ionic liquid solutions. *Chemical Society Reviews* **2012,** *41* (2), 829-868.